JCI The Journal of Clinical Investigation

Distinct mechanisms drive divergent phenotypes in hypertrophic and dilated cardiomyopathy associated TPM1 variants

Saiti S. Halder, … , William Lehman, Stuart G. Campbell

J Clin Invest. 2024. https://doi.org/10.1172/JCI179135.

Research In-Press Preview Cardiology

Graphical abstract

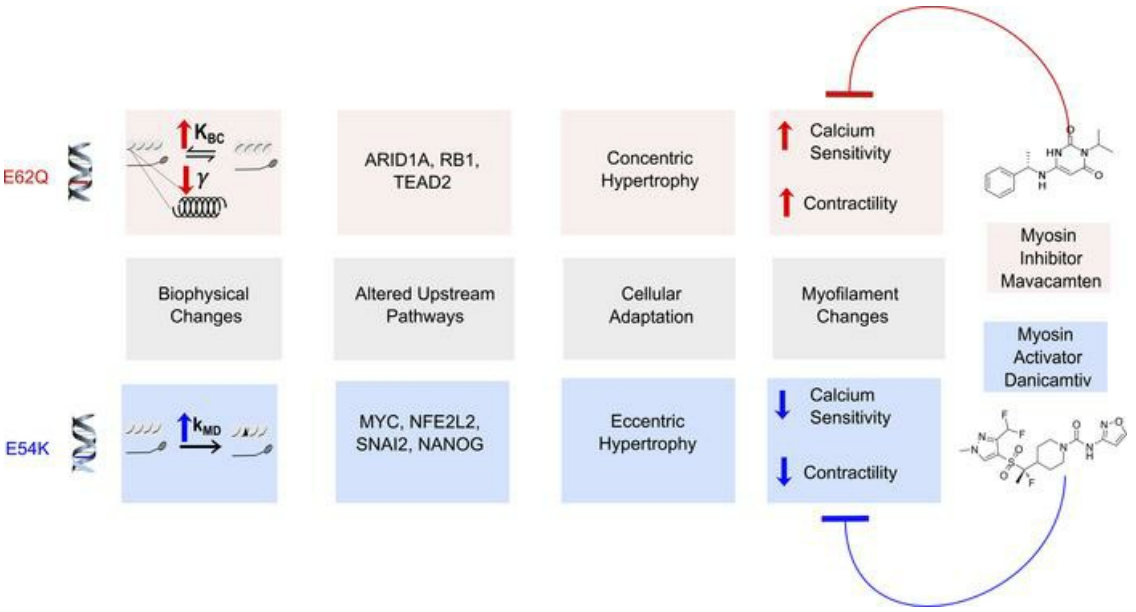

Distinct Mechanisms Drive Divergent Phenotypes in Hypertrophic and Dilated Cardiomyopathy associated *TPM1* variants

Saiti S Halder[1], Michael J Rynkiewicz[3], Lynne Kim[1], Meaghan Barry[3], Ahmed GA Zied[4], Lorenzo R Sewanan[1], Jonathan A Kirk[4], Jeffrey R Moore[3], William Lehman[3], Stuart G Campbell[1]

1. Department of Biomedical Engineering, Yale University
2. Department of Biological Sciences, University of Massachusetts Lowell
3. Department of Pharmacology, Physiology, & Biophysics, Boston University Chobanian & Avedisian School of Medicine
4. Department of Cell and Molecular Physiology, Stritch School of Medicine, Loyola University Chicago

Corresponding Author:

Stuart G Campbell

stuart.campbell@yale.edu

10 Hillhouse Avenue

PO Box- 208267

New Haven, CT- 06520-8267

Abstract (200 words)

Hypertrophic and dilated cardiomyopathies (HCM and DCM, respectively) are inherited disorders that may be caused by mutations to the same sarcomeric protein but have completely different clinical phenotypes. The precise mechanisms by which point mutations within the same gene bring about phenotypic diversity remain unclear. Our objective has been to develop a mechanistic explanation of diverging phenotypes in two *TPM1* mutations, E62Q (HCM) and E54K (DCM). Drawing on data from the literature and experiments with stem cell-derived cardiomyocytes expressing the *TPM1* mutations of interest, we constructed computational simulations that provide plausible explanations of the distinct muscle contractility caused by each variant. In E62Q, increased calcium sensitivity and hypercontractility was explained most accurately by a reduction in effective molecular stiffness of tropomyosin and alterations in its interactions with the actin thin filament that favor the 'closed' regulatory state. By contrast, the E54K mutation appeared to act via long-range allosteric interactions to increase the association rate of the C-terminal troponin I mobile domain to tropomyosin/actin. These mutation-linked molecular events produced diverging alterations in gene expression that can be observed in human engineered heart tissues. Modulators of myosin activity confirmed our proposed mechanisms by rescuing normal contractile behavior in accordance with predictions.

Graphical Abstract

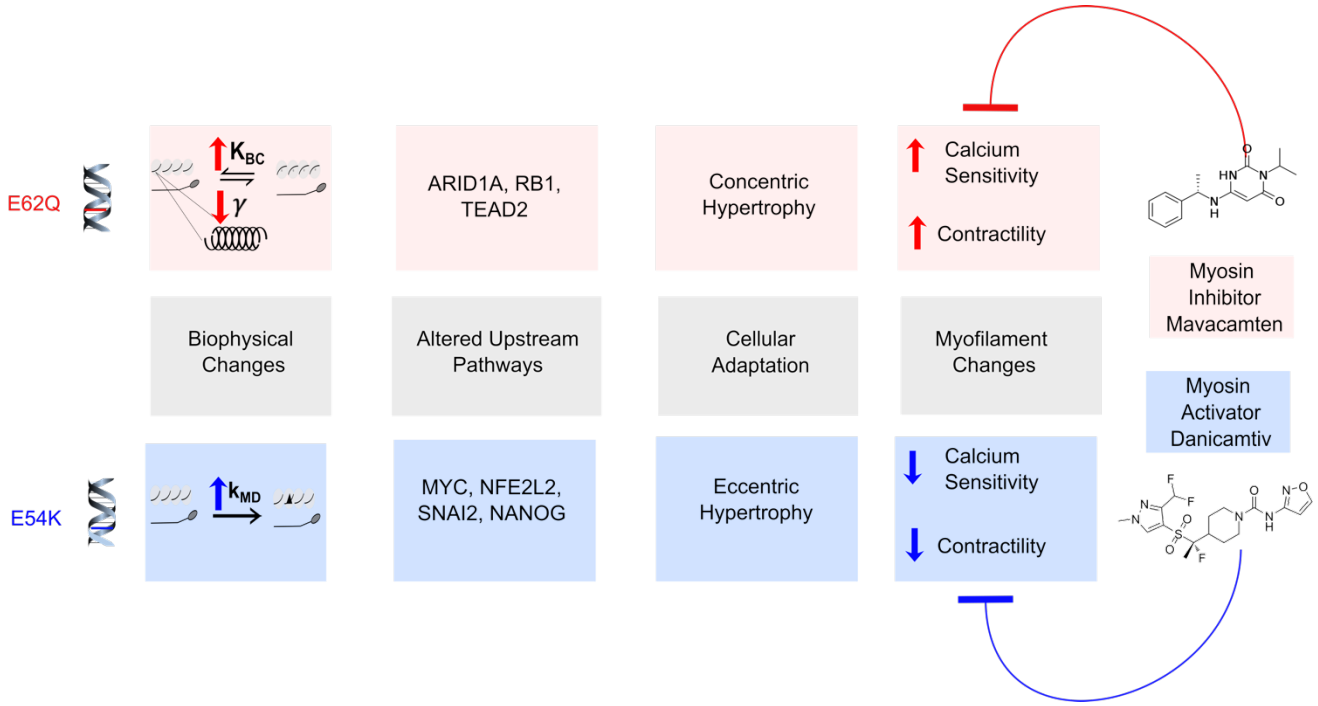

Introduction

Hypertrophic cardiomyopathy (HCM) and dilated cardiomyopathy (DCM) are two of the most common forms of genetic heart diseases and are a leading cause of sudden death and heart failure in otherwise young and healthy individuals (1). HCM is associated with thickening of the left ventricular wall, myocyte disarray and interstitial fibrosis (2) while DCM is a condition defined by thinning of the left ventricular wall, enlargement of the left ventricular chamber, reduced ejection fraction, and fibrosis (3). Despite being phenotypically divergent, both diseases have been linked to mutations in many of the same sarcomeric proteins of the thick and thin filaments. For instance, the R403Q, R453C, and K207N mutations in *MYH7* (myosin heavy chain) have been shown to cause HCM while S532P and F764L mutations in the same gene have been associated with DCM phenotypes (4). Similarly, over 30 HCM-causing mutations and 10 DCM-causing mutations have been identified in *TNNT2* (5), some of which are linked to the same protein residue. In the gene encoding alpha-tropomyosin (*TPM1*), the disease phenotypes associated with identified mutations are divided almost evenly between HCM and DCM.

Thus, considerable effort has been spent in attempting to distinguish the acute physiological effects of HCM vs. DCM mutations. In vitro motility assays using purified proteins, skinned muscle fiber preparations or membrane-permeabilized cells have been used frequently to identify and categorize functional differences caused by HCM or DCM mutations at an in vitro scale. These studies generally suggest that HCM mutations increase calcium sensitivity of actin/myosin activity while DCM mutations decrease it (6). However, there are exceptions to this paradigm. For example, these assays have shown that both R312C (HCM causing) and R312H (DCM causing) mutants in cardiac actin reduce calcium sensitivity (7). In

another case, high doses of the HCM-causing mutant *TNNT2* R278C administered to membrane permeabilized cells resulted in a rightward shift in force-pCa curve, indicating a decrease in calcium sensitivity (8). Therefore, alterations in calcium sensitivity are often not clearly predictive of disease phenotype.

In contrast, an arguably more physiologically relevant study in transgenic mice by Davis and colleagues generated a more consistent picture of HCM vs. DCM pathogenesis. Using transgenic mice expressing either HCM- or DCM-causing cTnC mutations, they measured the force-time integral (FTI, an index computed by integrating muscle isometric twitch force-time values) which served as a reliable predictor of phenotype (9). In their examination of isolated heart muscle preparations, mutations that caused increases in FTI, without exception caused left ventricular hypertrophy. Conversely, mutations that decreased FTI produced DCM.

To determine if the relationship between FTI and HCM/DCM phenotypes extends to mutants in TPM1, we undertook a comparison of HCM and DCM mutations in *TPM1* to serve as an extensively characterized simple model system. The two *TPM1* mutations chosen were E54K (DCM) and E62Q (HCM) based on their pathogenicity and extensive mechanistic characterization (6,10–13). Both are located on the same actin binding repeat of tropomyosin (14) and positioned only 8 amino acids apart. Their formal classifications as DCM- and HCM-linked, respectively is based on strong clinical evidence. E54K was identified as a novel mutation in 2001 in a study involving DCM patients. The familial proband died at age 27 while waiting for a heart transplant and their father and paternal uncle died at ages 27 and 49 both from heart failure. E62Q was first identified in 2003 in a large Dutch HCM family spanning 5

generations. Nine individuals in the same family died from sudden cardiac death at varying ages ranging from 15-47 years.

Hence, we engineered *TPM1*$^{E62Q/E62Q}$ and *TPM1*$^{E54K/E54K}$ mutations into the same wildtype human induced pluripotent stem cell line (iPSC). This enabled comparison of phenotypes on an isogenic background and in the context of human genetics. By seeding iPSC-derived cardiomyocytes into engineered heart tissues (EHTs), we were able to study physiologically relevant muscle function while excluding potentially confounding secondary effects caused by neuroendocrine control of cardiac function or other compensatory mechanisms. The choice to use *TPM1* variants for this study allowed a strong mechanistic basis on which to seek detailed explanation of mutation effects at the single molecule and residue-to-residue levels.

Our work reveals starkly diverging phenotypes and a diverse set of differentially expressed genes in these cases of HCM vs. DCM as well as specific, plausible molecular mechanisms by which the respective mutations provoke their unique phenotypes. These data and analyses confirm the notion that left ventricular hypertrophy can be driven by hypercontractility and dilation by hypocontractility, congruent with the hypothesis advanced by Davis et al. (9). Additionally, our conclusions are supported by demonstration that non-acute treatment of mutation-expressing EHTs with appropriate small molecules to counter aberrant myofilament behavior can correct disease phenotypes.

Results

Hyper- and hypo-contractility observed in E62Q and E54K EHTs

Three isogenic iPSC cell lines were used to study the impact of *TPM1* HCM/DCM mutations on cardiomyocyte function: WT, WT with a CRISPR/Cas9-induced homozygous $TPM1^{E62Q/E62Q}$ mutation (HCM-causing), and WT with a CRISPR/Cas9-induced homozygous $TPM1^{E54K/E54K}$ mutation (DCM-causing). These cells were then seeded onto decellularized porcine myocardium to fabricate engineered heart tissues which we used to evaluate the active contractile properties of the EHTs.

The mutant EHTs demonstrated drastically different isometric twitch phenotypes (Figure 1A and Figure 1B). E62Q EHTs produced a greater than three-fold increase while E54K EHTs demonstrated an almost three-fold decrease in the active peak force compared with WT (Figure 1C). Although the twitch kinetics did not vary significantly between E62Q and WT EHTs, E54K EHTs exhibited a shorter-lived twitch and took 42% less time than WT EHTs to reach peak force (Figure 1D) and only took half as much time as WT EHTs to relax (Figure 1E). The significant twitch kinetic differences in E54K compared to both E62Q and WT were also reflected in the reduced force time integral (FTI) (Figure 1F). Since impaired Frank Starling mechanism is often an indication of systolic abnormalities, we also measured the length-dependent activation of EHTs by assessing the peak force generated at various levels of tissue stretch (Figure 1G). We normalized the peak forces to each group's mean contractile force at culture length (0% stretch) to better visualize the relative length dependent activation (Figure 1H). We observed that there was little to no length dependent activation in E54K EHTs while E62Q EHTs showed similar length dependent activation as WT EHTs.

Diastolic Stiffness was drastically higher in E62Q EHTs

Having observed drastically different active isometric twitch properties, we chose to examine whether the biomechanical properties of tissues in between stimulated contractions (passive, or 'diastolic' properties) were also changed in the E62Q and E54K mutants. EHTs were slowly stretched from a slack length (−3% relative to culture length) to a stretch of 9%, while being electrically paced at 1 Hz (Figure 2A). The diastolic force in this case is defined as the minimum force level observed between stimulus events. E62Q EHTs showed a greater than 4-fold increase in diastolic stress across all stretch levels compared to WT while E54K EHTs seemed to be slightly more compliant than WT EHTs although this change was statistically insignificant (Figure 2B). We hypothesized that the increased diastolic stress may have been a result of incomplete inhibition of actin-myosin interactions during the diastolic interval. To test this, we subjected the tissues to a high concentration of mavacamten, a small molecule myosin inhibitor for 30 minutes and then re-measured length-dependent diastolic stresses. The acute drug treatment drastically reduced the diastolic stress in E62Q EHTs, compared to WT or E54K, resulting in a significant genotype-drug interaction ($p = 0.0001$) (Figure 1C) and indicating that the increased diastolic stress in E62Q EHTs could be attributed to the presence of residual actin-myosin crossbridges during the diastolic interval.

Divergent transcriptomic signatures of E62Q and E54K EHTs

Given the very divergent phenotypes exhibited by the two *TPM1* mutants in both systolic and diastolic assessments, we next sought to identify any accompanying changes in gene expression and cell signaling pathways. To that end, we performed bulk RNASeq on WT, E62Q and E54K

EHTs. A principal component analysis on the resulting data shows distinct clusters formed by WT, E62Q and E54K EHTs. We plotted the first (PC1) and third (PC3) principal components and noted that the mutant groups diverged from the WT cluster along PC1, but both shifted away from the WT cluster along PC3 (Figure 3A). This implies that PC1 represents the set of genes that are differentially expressed in HCM and DCM while PC3 represents the set of genes that are expressed differentially because of homeostatic imbalance regardless of whether the mutation is HCM- or DCM-linked. Differential expression analysis of transcriptomic data revealed that over 1500 genes were differentially regulated in both HCM and DCM compared with WT (Figure 3B and Figure 3C). To see what proteomic changes were occurring as a result of the *TPM1* mutations we performed mass spectrometry. Mass spectrometry also yielded over 800 differentially regulated proteins in both mutants (Figure 3E and Figure 3F). From the mass spectrometry data we queried the levels of various sarcomeric protein isoforms (Figure S3). Our EHTs exhibited no significant changes between mutant EHTs and WT EHTs in terms of *MYH6*, *MYH7*, *TNNI1, TNNI3 , TTN* and ratio of cardiac troponin I to total troponin I and beta myosin heavy chain to total myosin. HCM EHTs had significantly higher *MYL2* compared with WT EHTs. We next sought to investigate what pathways and signaling molecules were activated in each disease. We first performed upstream factor analysis independently on the proteomic and transcriptomic datasets. We used Qiagen Ingenuity Pathway Analysis to analyze which upstream transcription factors were activated or inhibited for each disease. Transcription factors which showed up in both independent upstream analyses are shown in Figure 3G. We then looked at the set of genes and proteins that were congruently upregulated or downregulated in the two datasets and then subjected this set to pathway analysis (Figure 3D). This revealed modulation of several canonical signaling pathways (Figure 3H), with HCM mutation impacting metabolic

pathways and DCM mutation impacting extracellular matrix reorganization and fibrotic pathways.

Differences in 2D Cardiomyocyte Morphology

Given the divergent transcriptomic signatures of the mutant EHTs, and enrichment of canonical pathways that are consistent with changes in cell morphology such as oxidative phosphorylation and mitochondrial dysfunction (15) we next sought to investigate whether cell morphology was changing in our disease models as well. Because it is difficult to calculate cell size accurately when seeded onto scaffolds, we cultured differentiated cardiomyocytes in sparse 2D monolayers. We noticed that even in a simple culture milieu, there were drastic changes in the morphology of mutant cardiomyocytes (Figure 4A-C). Upon analyzing the images, we found that the average cell area was more than 2-fold higher in E62Q cells compared with WT, while E54K cells were not significantly different in size (Figure 4D). E54K cells, however, were more elongated and had a 3-fold higher aspect ratio (ratio of major to minor axis of fitted ellipse) compared to both WT and E62Q EHTs (Figure 4E).

Plausible mechanisms of pathogenicity in E62Q and E54K can be identified using computational models

Having observed robustly different expressions of morphological phenotypes in 2D cardiomyocytes as well as functional phenotypes in 3D EHTs, we next aimed to identify the fundamental mechanism linking the diseased phenotypes to their respective genotypes. One well established fact is that both these mutations alter calcium sensitivities as measured by in vitro motility assays or thin filament reconstituted skinned muscle fibers. Results from previous studies that were used in subsequent analysis are summarized in Table 1 which shows higher

calcium sensitivity in E62Q and lower calcium sensitivity in E54K. We confirmed these shifts in calcium sensitivity by performing our own regulated in vitro motility assays on both mutants (Figure S1).

To understand how the two mutations could plausibly exert their respective effects on myofilament calcium sensitivity, we used a 24-state Markov model of thin filament function previously published by our group (16). This model is based on current understanding of tropomyosin's role within the thin filament regulatory switch as well as its binding interactions with other sarcomeric proteins. We encapsulate tropomyosin function in terms of four fundamental model parameters as follows: Tropomyosin stiffness (γ) is an intrinsic molecular property which affects cooperative spread of thin filament activation. The blocked-closed equilibrium constant (K_{BC}) is determined largely by electrostatic interactions between tropomyosin and actin and describes the relative equilibrium of tropomyosin between its primary actin regulatory states. It is important to note that in this model, changes in the blocked-closed equilibrium constant (K_{BC}) are implemented as adjustments in the forward kinetic rate (B to C) and as such, appropriately modulates both steady state and dynamic responses. The association rate of troponin-I mobile domain to tropomyosin/actin (k_{MD}) is a key regulatory step in Ca^{2+} activation of the thin filament. Finally, as myosin binds to the thin filament and undergoes its power stroke, it interacts with and displaces tropomyosin into its open (M) regulatory state. Hence, alterations in tropomyosin may affect the myosin crossbridge duty cycle (δ), which is the proportion of time myosin spends attached to the thin filament during its cycle (Figure 5A). Our goal was to seek a set of mutant tropomyosin parameter changes that could simultaneously explain the steady-state and isometric twitch alterations associated with each mutant.

We first set the parameters of the model to match literature values of WT calcium sensitivity (pCa_{50}) and cooperativity (n_H). Then we applied changes in the parameters representing distinct hypotheses to see which could match literature values of calcium sensitivity (pCa_{50}) and cooperativity (n_H) associated with each mutation. Subsequently, we applied the same proportional change in parameters that provided the best description of the calcium sensitivity to simulate isometric twitches and compared the simulations with our experimental results (Figure 5B).

Contractile phenotypical divergence in HCM- and DCM-linked mutations may be explained by different underlying mechanisms

For each hypothesis described in Figure 5B, we changed only the parameters in question relative to the WT parameter set while leaving all other model parameters constant. The parameter values that most accurately reflected the change from WT to mutant calcium sensitivity (pCa_{50}) and cooperativity (n_H) values were recorded (Figure 6A, Figure 6B). All steady state simulations done for E62Q yielded perfect matches with literature values for calcium sensitivity (pCa_{50}) for the parameter changes shown. However, cooperativity (n_H) values could only be matched using multi-parameter hypotheses. In the case of E54K, single parameter changes to γ, K_{BC} or δ could not match in vitro measurements. Among the remaining hypotheses, all except the $\gamma + \delta$ hypothesis yielded perfect matches with literature values for calcium sensitivity (pCa_{50}). In general, it was more difficult to obtain good cooperativity (n_H) matches for E54K across all hypotheses, with only the k_{MD} providing a reasonable fit.

Having generated multiple parameter sets capable of explaining steady-state data, we sought additional refinement of candidate mechanisms by determining which might also produce reasonable predictions of isometric twitch force measurements (Figure 1). For E62Q, isometric twitch simulations of all hypotheses generated peak forces lower than measured experimental values but with the γ + K_{BC} hypothesis coming the closest with a 1.5-fold increase. Our experimental results showed no change in TTP and RT50, a scenario which was also most accurately reflected by the γ + K_{BC} hypothesis. The γ-only, K_{BC}-only and K_{BC} + γ + δ hypotheses matched RT50 but not TTP. The three-fold increase in baseline force measured by in vitro experiments was also most accurately reflected by the γ + K_{BC} hypothesis.

For E54K, where experimental results showed shorter-lived and hypocontractile twitches, the k_{MD} only, and k_{MD} + γ hypotheses simulations offered the closest matches across all metrics. Among these two, the k_{MD} only hypothesis recapitulated experimental results most accurately. Based on these semi-quantitative comparisons, we found the best explanation for the effects of E62Q to be a decrease in tropomyosin's molecular stiffness (γ) combined with altered tropomyosin-actin electrostatics such that the blocked-closed equilibrium (K_{BC}) was shifted toward the closed state. The functional effects of E54K seem best and most simply explained by an increased affinity of tropomyosin for the cTnI mobile domain (k_{MD}). The steady-state simulations and isometric twitch simulations for each winning hypothesis are shown in Figure 6C and Figure 6D for E62Q and E54K respectively.

Atomistic simulations provide qualitative and quantitative evidence to support proposed mechanisms

Having identified plausible molecular-level characteristics describing each mutation's effect on contractile phenotypes, we sought supporting evidence by examining structural models of tropomyosin and the thin filament. Our model fits suggested a drop in tropomyosin stiffness as a potential mechanism for E62Q. We therefore used molecular dynamics simulations of the tropomyosin molecule and fed the observed local angular fluctuations along its axis into a previously published coarse-grain model (17) to estimate the effective tropomyosin chain stiffness. The chain energy calculated over a range of azimuthal displacements (Figure 7, left) demonstrated a 21% drop in tropomyosin stiffness when E62Q is introduced (compared with WT). The model predicted a 57% reduction in tropomyosin stiffness. While the magnitude of the change is different, the directionality of the change is consistent.

The other molecular change we hypothesized from the model fits to E62Q data was an increase in the blocked-closed equilibrium constant K_{BC}. We examined the Protein Database structures (PDB ID: 7UTI and 7UTL) of WT tropomyosin in the presence and absence of calcium (Figure 7, middle). In the low calcium state, tropomyosin residue E62 is close to K328 and R147 on actin. Mutating the charged residue to a polar one would presumably weaken this interaction, thus destabilizing the B-state and making the filament easier to turn on (18). This is precisely what was represented in the model by an increase the K_{BC} parameter.

For E54K, we measured the B State electrostatic tropomyosin- troponin I interaction energies using atomistic simulations. Molecular dynamics simulations in explicit solvent were

performed twice comprising 4 independent replicas modeled with the E54K mutation. Statistical analysis shows that interaction energies for tropomyosin and the mobile domain of troponin I are significantly more negative when E54K is introduced compared with WT (Figure 7, right). The more negative values suggest an increased association energy or affinity of the troponin I mobile domain to tropomyosin/actin. This is precisely the molecular effect that reproduced the main features of steady-state and twitch activity in our simulations of E54K.

Confirming downstream pathogenic mechanisms in mutant EHTs

It is notable that even our best-performing simulations tended to underestimate peak twitch force changes in the case of E62Q (HCM) and overestimate them for E54K (DCM) (Figure 6). As we showed in previous work on *TPM1* variant S215L (19), we believe that this is because the model represents acute mutation effects only and does not account for their chronic impacts on cell size and morphology that emerge over time (Figure 4). Ultimately, peak force measured in EHTs is reflective not only of direct mutation changes in myofilament behavior but also due to downstream, chronic changes in myofilament content or arrangement within cardiomyocytes that exacerbate functional changes.

Thus, we hypothesize that counteracting the acute hyper- or hypo-contractile mutational effects in EHTs should be sufficient to correct the chronic changes in peak force caused by cellular remodeling.

To test this hypothesis, we turned to cardiac myosin-specific small molecule modulators that provide a targeted means of either enhancing or inhibiting myofilament contraction. Because it

was not certain that myosin modulators could rectify twitch force abnormalities caused by tropomyosin mutations, we first examined these scenarios in simulations of isometric twitches. We represented the action of myosin inhibitors or activators by adjusting the parameter for myosin binding to actin (f_{XY}) (Figure 8A). The model predicted that a myosin inhibitor could effectively reverse the hypercontractile effects of the E62Q mutation, restoring the peak force to WT levels with minor reduction in time to peak. On the other hand, the hypocontractile twitch of a E54K mutation was reversed by a myosin activator, with some increase in relaxation time.

Confident that myosin modulators could appropriately counteract acute effects of the tropomyosin mutations, we proceeded to test whether non-acute application to mutant EHTs would reverse phenotypical abnormalities. We designed an experiment where at the end of the usual culture period, we subjected our EHTs to 4 days of additional drug-supplemented media followed by a 24-hour washout (Figure 8B). We confirmed using LC-MS analysis that a 24-hour washout eliminated 85% of both compounds from drug-treated EHTs (Figure S2). We observed that for E62Q, a 0.5 μM 4-day treatment with the myosin inhibitor mavacamten was able to reduce peak force to WT levels, with minimal changes in twitch kinetics. Similarly, a 0.5 μM 4-day treatment with the myosin activator danicamtiv was able to raise peak force to WT levels in E54K EHTs.

These results confirm our conclusion that EHT contractility reflects both chronic and acute mutation effects. If mutation-dependent changes in EHT peak force were solely due to the direct biophysical consequences of the amino acid substitution, the contraction phenotypes we originally observed should have been completely restored following wash-out of the myosin

modulating drugs. However, 24 hours after wash-out the peak forces produced in mutant tissues most closely resembled those of the non-mutant controls and had not returned to levels associated with the un-treated mutants (Figure 8).

The other important conclusion furnished by this 4-day drug treatment is that it supports our proposed mechanistic pathways between each mutation and their resulting phenotype. That is, we assert that the E62Q mutation increases tropomyosin flexibility, destabilizes the blocked state of the thin filament, and consequently elevates contraction force beyond normal intrinsic levels, and finally provokes a cellular hypertrophic response. The link between hypercontractility and hypertrophy is confirmed by the fact that reducing contractility through mavacamten resulted in a durable reduction in twitch force in E62Q tissues. In like manner, the chronic hypocontractility measured in E54K mutant tissues was counteracted by administration of the myosin activator danicamtiv, which neutralized the tendency of E54K to suppress contraction.

Discussion

In this study, we undertook a thorough multiscale analysis of two *TPM1* mutations associated with diverging ventricular phenotypes. The objective was to use this unique comparison to expose fundamental differences in the pathogenic mechanisms of HCM and DCM. Our data provide support to the paradigm that mutations which cause intrinsic elevation of actin-myosin contractility provoke cardiomyocyte hypertrophy, while those which intrinsically decrease contractility lead to cardiomyocyte lengthening without hypertrophy (4,20,21). Unbiased gene

expression data confirm extensive differential pathway activation stemming from the distinct biophysical changes induced by E62Q and E54K within tropomyosin and the thin filament complex. Small molecule treatments that neutralized these respective mutation-induced defects dramatically resolved chronic contractile phenotypes. To our knowledge, this is the first time HCM and DCM mechanisms have been directly compared at this level of detail and within a human context.

HCM-causing mutation E62Q and DCM-causing mutation E54K have been studied extensively in previous work. However, in many aspects these studies report conflicting interpretations or fail to establish a clear mechanism. E62Q was first reported in 2003 linked to several cases of HCM in a multi generation Dutch family with an estimated penetrance of 75% and disease frequency of 0.2% (22). Subsequent studies have shown E62Q tropomyosin to confer greater sensitivity to calcium and an impaired ability to inhibit actomyosin ATPase activity (23,24). While some studies have found evidence of weakened actin-E62Q tropomyosin interaction (10,11,25) others found no difference in F-actin binding affinity of E62Q using actin-tropomyosin co-sedimentation assay (26). In silico studies have previously shown higher global flexibility of E62Q tropomyosin, and decreased persistence length (25). In our EHTs, E62Q showed a three-fold increase in peak force without any changes in kinetics and no difference in the length dependent activation. The hypercontractile feature (19,27–29) and impaired Frank-Starling mechanism (19,28) is common to many other reported variants of HCM. Similar to previous studies with HCM-associated tropomyosin mutants E192K and S215L (19,27), E62Q showed an increase in diastolic stiffness. Atomistic simulations of tropomyosin showed that each of these mutations caused bending stiffness of the molecule to be less than wildtype. In the

context of thin filament regulation, reduced tropomyosin stiffness prevents cooperative inhibition of myosin binding sites on actin under low Ca2+ conditions, leading to residual crossbridge activity during the diastolic interval. At the level of the intact heart, it is therefore anticipated that reduced tropomyosin stiffness would lead to greater resistance to ventricular filling.

By contrast, E54K was identified as a novel mutation in 2001 in a study involving DCM patients (30). Several studies have shown a decrease in E54K tropomyosin calcium sensitivity (12,23,31) while others have reported no change compared with WT (6,32). These biophysical changes have proven to have physiological consequences. Transgenic mice expressing E54K tropomyosin demonstrated impaired systolic and diastolic function (13). In our EHTs, E54K exhibited strikingly different isometric twitch profiles from E62Q. In the case of E54K, we observed a hypocontractile, short-lived twitch with essentially no length dependent activation. This is reminiscent of the study by Schwinger et al. where skinned muscle fibers obtained from terminally failing myocardium with DCM have shown complete failure to exhibit the Frank-Starling mechanism (33). In contrast with HCM-linked variants, the DCM-associated E54K tissues were very compliant. This reduced passive stiffness may be due to a shift towards the longer, more compliant N2BA isoform of titin that is predominant in DCM (34,35).

The drastic differences in functional phenotypes encouraged us to look at the transcriptomic changes that were present in mutant tissues. Bulk RNA-Seq and Mass Spectrometry analysis revealed distinct transcriptomic and proteomic signatures in HCM and DCM. Because transcriptional changes do not always result in protein level changes, we focused on genes and proteins that were regulated in tandem. Independent analysis of both datasets revealed a handful

of upstream transcriptional regulators that were synonymously altered. In HCM, both transcriptional and proteomic datasets suggested activation of *ARID1A* and *TEAD2* associated genes and inhibition of *RB1* associated genes. *ARID1A* plays a role in ischemic heart disease by suppressing cardiac proliferation (36). Inhibition of *RB1* has been shown to induce cardiac hypertrophy (37). *TEAD2* (also known as Transcriptional Enhancer Factor or TEF-2) plays a key role in muscle differentiation and development. Several kinases that are involved in hypertrophic pathways such as protein kinase A and protein kinase C can post-translationally modify TEAD proteins (38,39). *TEAD2* therefore may play an important role in HCM and DCM disease progression. In DCM EHTs, *MYC* and *NFE2L2* associated genes were activated, while *SNAI2* and *NANOG* associated genes were inhibited. Proto oncogene *MYC* encodes c-Myc which is a potential therapeutic target for cardiomyopathies (40). *NFE2L2* is the gene encoding transcription factor NRF which mediates oxidative stress response and plays a key role in cardiac protection (41). *SNAI2* is a transcription factor that is crucial for atrioventricular development (42).

Several other pathways were shown to be altered by HCM/DCM in the analysis of proteomic and transcriptomic data, such as oxidative phosphorylation, fibrosis and mitochondrial dysfunction, all of which have previously been differentially regulated in cardiomyocytes with altered aspect ratios (15). This encouraged us to look at potential changes in cell sizes in mutant cardiomyocytes. 2D stained images demonstrated that even in the absence of hormones, hemodynamic load, or adrenergic stimulus, E62Q cells exhibited a sharp increase in cell size while E54K cells had an elongated morphology. It has been stipulated before that pathological remodeling in adult hearts in response to chronic pressure overload results in concentric

hypertrophy where sarcomeres are added in series while a chronic volume overload would result in eccentric hypertrophy where sarcomeres are added in parallel (43). However, it may be possible that cardiomyocytes have an intrinsic force-morphology homeostatic pathway that is independent of hemodynamic or adrenergic regulation.

Having characterized the divergent functional, transcriptomic, and morphological changes that occur as a result of E62Q and E54K mutations, we then focused on identifying the most immediate biophysical impact of the genetic insult. To that end, we devised several hypothetical changes in model molecular parameters through which mutant tropomyosin might impact thin filament regulation and tested them using our computational model. For the HCM mutant E62Q, the hypotheses that best matched our experimental data was a drop in tropomyosin stiffness combined with an increase in blocked-closed equilibrium constant. Consistent with these model parameters being key to the phenotype, atomistic simulations indicate that E62Q can reduce effective tropomyosin stiffness. Furthermore, in the blocked state E62 engages in interactions with actin residues, which stabilize the off state. These interactions would either be weaker or more transient or may not be formed altogether by Q62; thus, an E62Q-induced destabilization of the blocked state can lead to an increase in the blocked-closed equilibrium constant, as precited by our comprehensive modelling.

In the case of E54K, unlike E62Q, there are no direct contacts between actin or troponin and tropomyosin in the structure, therefore, the pathogenic mechanism likely propagates via long-range allosteric interactions that result in an increase in the association rate of the troponin I mobile domain to tropomyosin/actin. This proposed mechanism for E54K has never been

suggested before for any DCM tropomyosin mutant. Local residue changes to the coiled coil structure of tropomyosin can result in long-range alterations in tropomyosin structure even up to a few hundred angstroms away from the original site of the mutation (11,44,45). Molecular dynamics simulations show that E54K tropomyosin-TnI interactions are more stable in the B-state compared to WT tropomyosin-TnI interactions, validating this notion (Figure 7, right).

Interestingly, however, given the likelihood of a generic force sensing mechanism inherent to cardiomyocytes, the specific mechanism driving the pathogenicity may not be consequential in terms of treatment. We tested this theory in our computational models by altering myosin activation/inhibition to correct the phenotype and observed a reversal in the contractility. A 4-day treatment with myosin activators/inhibitors was able to achieve phenotype rescue even after 48 hours of washout, which explains the success of small molecule myosin modulators in a clinical setting regardless of underlying causes of HCM or DCM (46–49).

Our study is certainly not without limitations. Although EHTs made from human iPSC derived cardiomyocytes offer an excellent testing bed for many physiologically relevant questions, the isolated system lacks hemodynamic load, or adrenergic control which can impact tissue function. Our proposed hypotheses only represent a subset of myriad possible mechanisms that we either assumed to be unlikely or are not easily implementable using our existing model. The best fit for our computational simulations were matched to literature data which are in vitro experiments that have their own limitations and values may not be comparable across studies. Previously, we showed that there was a linear correlation between gene dosage and phenotypic severity of TPM1 mutation S215L (19). It is important to note that in this study we only tested homozygous

mutations in order to accentuate the differences. We anticipate that the more clinically relevant heterozygous mutation would behave similarly but have a milder effect. Moreover, this study only analyzes one HCM and one DCM mutation in depth. Future work should involve testing this paradigm on a broader range of thin filament mutations.

Despite the limitations, this study clearly demonstrates divergent trends in E62Q and E54K mutants across several spatial scales and uncovers important insights. The first is that mutant cardiomyocytes alter their morphology likely due to an inherent force sensing mechanism that detects a departure from a homeostatic setpoint. Secondly, there are key upstream regulators that may be responsible for driving the transcriptomic changes at an early stage. Thirdly, the two mechanisms likely propagate via very different mechanisms. And finally, a mechanism agnostic approach is effective in rescuing the phenotype.

Methods

Sex as a biological variable

Sex was not considered as a biological variable in this work. All experiments were conducted using three isogenic cell lines originally derived from a human male patient (GM23338, Coriell Institute).

iPSC maintenance and differentiation

Isogenic cell lines were created by the University of Connecticut Health Sciences Human Genome Editing Core, using CRISPR/Cas9 to introduce the *TPM1*$^{E62Q/E62Q}$ and *TPM1*$^{E54K/E54K}$ variant into a commercially available WT human induced pluripotent stem cell (iPSC) line (GM23338, Coriell Institute). Upon delivery, the iPSCs were differentiated into ventricular cardiomyocytes ((50)). First, iPSCs were plated on a Matrigel (Corning, 1:60 diluted) coated well for culture for 3–4 days in mTeSR medium (Stemcell Technologies, 05850) till ~90% confluency and treated with 20 μM CHIR99021(Selleckchem) on day 0 for 24 h and 5 μM IWP4 (Stemgent) on day 3 in RPMI (Gibco)/B27 (Gibco) minus insulin media for 48 h. During the cardiac differentiation, media were changed every other day with RPMI/B27 minus insulin media. After beating, cardiomyocytes were cultured in regular RPMI/B27 (including insulin). Cardiomyocytes at day 14 were treated with 4 mM lactate (Sigma) in glucose-free medium for 4 days to obtain enriched CMs.

Cell Size Measurements

Differentiated cardiomyocytes at day 18 were passaged at a low concentration onto Matrigel coated 12-well tissue culture plates. The cells were cultured in RPMI/B27 (including insulin) for 4 days after which they were fixed using 4% paraformaldehyde overnight at 4°C before immunostaining. The primary cardiac TnT antibody used was MS-295 p0-(Thermo Fisher) at a dilution of 1:500. The secondary antibody used was goat anti-mouse IgG, Alexa Fluor 488 (Thermo Fisher, A-11029) at a dilution of 1:300. The cells were incubated for 1 h in secondary antibody and Hoescht dye (NucBlue, Thermo Fisher) before imaging under an inverted

fluorescent microscope at 40X. Images were analyzed using ImageJ to calculate area and aspect ratio for each cell. Image J calculates aspect ratio as the ratio of major axis to minor axis of the fitted ellipse.

Fabrication of Engineered Heart Tissues

EHTs were made by seeding iPSC-CMs into decellularized porcine myocardial slices according to our previously published protocol (51). Briefly, 150 μm thick slices were obtained from porcine left ventricular free-wall blocks, mounted onto custom tissue culture cassettes and decellularized. The scaffolds were then treated with 10% FBS and 2% antibiotic-antimycotic (Thermo Fisher) overnight. iPSC-CMs were dissociated using TrypLE Express 1x (Thermo Fisher) followed by washing with PBS and manual pipetting. For this study, we seeded WT, E62Q and E54K cell suspensions containing 1 million cells onto each scaffold and allowed them to incubate overnight. The EHTs were subsequently grown in DMEM + 2% B27 plus insulin for 14 days. EHTs were then harvested for RNA sequencing or evaluated mechanically.

RNA Sequencing

For RNA extraction, tissues were flash frozen and crushed with plastic pestles. The aqueous phase was collected after TRIzol (Ambion) phase separation, and the RNA pellets were precipitated for total RNA extraction. Samples were treated with DNAse and cleaned with Qiagen RNeasy columns. Samples were sequenced by Yale Center for Genomic Analysis

(Illumina HiSeq 2500, multiplexed, paired-end reads of 100 base pair length with 25 million reads per sample). Data analysis was performed on PartekFlow. Alignment was performed using STAR 2.7.8a and hg38 as the reference genome. Samples were clustered by average linkage using Pearson's dissimilarity. Differential analysis was performed using DESeq2 and genes with $p < 0.05$ and fold change less than or greater than 1.5 were filtered. Pathway analysis was performed using the Ingenuity Pathway Analysis software (Qiagen) with the filtered dataset. Top relevant canonical pathways with a p value of <0.05 were considered. Upstream analysis was also performed using Qiagen Ingenuity Pathway Analysis Software and top transcription factors with the highest Z score and lowest p-values were identified.

Mass Spectrometry

EHTs were resuspended in 9M Urea (Millipore Sigma) and sonicated. Protein concentration was determined using a BCA assay (Thermo Fisher). 100ug of protein per sample was used for in-solution digestion. Samples were reduced with 5mM DTT for 45 min and then alkylated by incubation in 10mM iodoacetamide for 30 min. The proteins were digested next with 5 ug Trypsin/LysC protease for 18 h at 37 °C. The reaction was stopped by adding TFA at 0.1% final volume to bring the pH under 3. Samples were then dried by vacuum centrifugation, reconstituted in buffer A (3% acetonitrile, 0.1% formic acid) and analyzed by liquid chromatography tandem mass spectrometry (LC-MS/MS).

Purified peptides concentration was measured using Pierce™ Quantitative Peptide Assay (Thermo Fisher) and 1.0 ug were loaded onto a Vanquish Neo UHPLC system (Thermo Fisher) with a heated trap and elute workflow with a C18 PrepMap, 5mm. Spectra were acquired with an Orbitrap Eclipse Tribrid mass spectrometer with FAIMS Pro interface (Thermo Fisher

Scientific). Raw data were analyzed using Proteome Discoverer 2.5 (Thermo Fisher) using SEQUEST-HT search engines. The data were searched against the *Homo Sapiens* UniProt protein sequence database (UP000005640). The search parameters included precursor mass tolerance of 10 ppm and 0.6 Da for fragments, allowing two missed trypsin cleavages. Oxidation (Met) and acetylation (protein N-term) and phosphorylation (+79.966, STY) were set as variable modifications, and carbamidomethylation (Cys) as a static modification. Normalization was based on total peptide Amount; low abundance peptides were removed by filtering out proteins with less than 3 PSMs. Protein abundance calculations were based on the summed abundance of the connected peptide groups, and protein ratio was calculated as the median of all possible peptide ratios between replicates of all connected peptides. T-test was used for class comparison.

Active and Passive Mechanical Measurements

EHTs were assessed for their active contraction mechanics using a custom-built setup that utilizes a World Precision Instruments (WPI KG7) force transducer. The EHTs were kept in Tyrode's solution at 36°C and 7.4 physiological pH as they were paced at 1 Hz and stretched from culture length (0% stretch) to up to 10%. The resulting isometric twitch was analyzed in MATLAB to calculate peak force, time from stimulus to peak contraction, time from peak to 50% relaxation, and normalized tension-time integral. To characterize intracellular calcium dynamics, some EHTs were loaded with the ratiometric fluorescent indicator Fura-2 AM (Millipore) by incubation at room temperature for 20 min in loading solution (Tyrode's solution with 17 μg/mL Fura 2-AM, 0.2% Pluronic F127, and 0.5% Cremophor EL) and subsequently imaged at 36°C using a photometric system as previously described (51).

For passive mechanical measurements, EHTs were preconditioned by stretching them repeatedly, from slack length (−3% stretch) to a maximum stretch of 9% for three cycles at a rate of 0.015 mm/s (0.25% muscle length/s). After preconditioning, EHTs were paced at 1 Hz and the force was recorded as they were stretched from −3 to 9%. The diastolic force produced was extracted by a custom MATLAB script as previously described (52). To assess the effect of acute mavacamten treatment on EHTs, passive diastolic force was measured prior to addition of mavacamten. Tissues were incubated at 36°C in 2 μM mavacamten in Tyrode's for 30 min while being paced at 1 Hz. Passive diastolic force was measured again after incubation once the active force had equilibrated.

Optical coherence tomography (OCT) scans were performed on tissues to capture the cross-sectional area which was then calculated using ImageJ. The cross-sectional area was used to normalize the passive force measured and therefore calculate the passive stress of the tissues.

Computational Simulations

We used a 24-state Markov model previously described by Creso and Campbell to predict changes in steady state and isometric twitch conditions (16). Briefly, the model simulates the behavior of 26 regulatory units in series, tracking for each unit the states of tropomyosin and key domains of troponin C and troponin I. The simulations use either a steady-state Ca^{2+} concentration or a transient to elicit contractile activity over a set time interval. Force was output as the number of regulatory units in a myosin-bound state.

To simulate in vitro motility assay (IVMA) data, steady-state force values at various Ca^{2+} concentrations were obtained by simulating a 5 second interval to ensure attainment of steady-

state conditions. The steady-state force was determined by averaging force over a window of the final 25% of each simulation. To convert these force values into sliding filament velocity, a simple proportionality (effective filament viscosity) between force and velocity was assumed (16). Steady-state force values at different Ca^{2+} concentrations were used to produce velocity-pCa plots which were fit using the Hill equation. For WT steady state simulations model parameters were chosen such that the steady state behavior matched previous literature in terms of pCa_{50} and n_H (11,12). Next, for each hypothesis being investigated only the relevant parameters were changed until the mutant steady state behavior in the literature were replicated. For a few of the hypotheses that involved a single parameter change, there was no solution that perfectly matched both pCa_{50} and n_H literature values and in those cases the parameter change reflecting the closest match to pCa_{50} was selected. For each hypothesis, we recorded the % change in the parameters that yielded best match to literature in terms of steady state behavior.

For isometric twitch simulations of WT, parameter sets were chosen such that twitches recapitulated similar characteristics as WT EHTs previously seen in literature (16,19). Then we applied the same proportional changes in parameters recorded earlier for each competing hypothesis to predict isometric twitch forces. The complete parameter sets are shown in Table 2. Twitch events were simulated by allowing the system to reach steady state at a diastolic Ca^{2+} concentration of 0.1 μM. The Ca^{2+} concentration was then allowed to produce a transient by increasing up to 1 μM based on data from Stull et al (53).

Model scripting and data post-processing was conducted in MATLAB, while the Markov chain-Monte Carlo algorithm was implemented in CUDA C++ for parallel processing. Simulations were executed on an Nvidia GeForce RTX 2080Ti graphics processing card.

To ensure convergence of the stochastic model, the simulation time course was repeated 1920 times on the GPU and the average force at each time step was calculated. To further reduce stochastic noise, twitch simulations were run 10 times and averaged to calculate twitch properties (diastolic force, peak force, time to peak force, and time to 50% relaxation).

Molecular Dynamics

Molecular dynamics simulations of isolated tropomyosin dimers were performed as previously described (54). The starting model was an ideal coiled-coil backbone where the tropomyosin side chains had been built to match crystal structure coordinates (55,56). After the E62Q mutation was incorporated, the structure was minimized in CHARMM using the CHARMM 27 force field and the GBSW implicit solvation model. Simulations were then run for 30 ns at 300 K with a frictional drag of 1/ps applied to solvent-exposed heavy atoms, a time step of 2 fs, and the SHAKE algorithm. The local superhelical changes in tropomyosin flexibility (δ angle) were calculated in CHARMM as described (54).

For simulations of E54K on an actin filament, the mutation was incorporated into the starting model wild-type model that had been subjected to 30 ns of simulation as previously described (19) consisting of 28 actin monomers, 8 tropomyosin chains, 4 troponin T chains, and 2 troponin I chains in explicit solvent containing 0.15 M NaCl and 3 mM magnesium chloride with the Mutator plugin in VMD (57). The solvated E54K system was then minimized in NAMD (58) in the CHARMM 36 force field. For simulation, the system was then heated to 300 K over 30 ps using Langevin temperature control and equilibration over the next 500 ps constant volume with gradual release of constraints on protein atoms. At this point, a short run of 100 ps was performed with the Langevin piston turned on to bring the system pressure up to 1 atm. For the production runs, the barostat was turned off, a constraint on the non-surface actins was applied

throughout with a force constant of 0.1 kcal/mol/Å^2 to maintain actin filament structure, and the simulation was run at constant volume for 30 ns and the results compared with the wild-type simulation as run from 30-70 ns. Interaction energies between tropomyosin and actin were calculated using the NAMDEnergy plugin in VMD with default settings. E54K simulations were performed on three separate B-state runs, giving a total of six independent tropomyosin copies for analysis.

Drug Treatment

For treatment of EHTs with drug, EHTs were grown to 21 days in DMEM and then subjected to 4 days of media supplemented with 0.5 μM mavacamten, 0.5 μM danicamtiv or DMSO vehicle, changed every 2 days. On the fourth day, media were removed, and EHTs were washed twice with media. EHTs were then grown in this drug-free media for 24 h before functional testing was conducted as before.

Statistics

Results are given as the mean with standard deviation. For a comparison of two groups, statistical significance was determined using 2-tailed Student's t-test with a confidence level of $p<0.05$. For paired analysis with repeated measurements on the same samples, paired t-tests were used with a confidence level of $p<0.05$. For comparison of groups under a single condition, 1-way ANOVA was used followed by pairwise comparison using post hoc testing with Tukey correction to determine significant differences with a confidence level of $p<0.05$.

For comparison of groups under multiple conditions, 2-way ANOVA was used followed by pairwise comparison using post hoc testing with Tukey correction to determine significant differences with a confidence level of $p<0.05$.

Bootstrap analysis (59) was performed to analyze the Molecular Dynamics data in Figure 7C. This analysis was run on MATLAB (code adapted from https://courses.washington.edu/matlab1/Bootstrap examples.html) with 10,000 repeated samplings.

Study Approval

No animal testing was involved in this study and therefore did not require any approvals.

Data Availability

All data generated or analyzed during this study are included in this published article and its supplementary information files. RNA Sequencing data can be found on the Gene Expression Omnibus (GEO) database (https://www.ncbi.nlm.nih.gov/geo/) under accession ID GSE251993. Mass Spectrometry data can be found on the MassIVE repository (https://massive.ucsd.edu/) under dataset identifier MSV000095377. Raw data for each experiment can be found in the Supporting Data Values file.

Author Contributions

S. Halder, L.R. Sewanan, S. Campbell, J. Moore and W. Lehman contributed to the study design. S. Halder, M. Rynkiewicz, and L.Kim contributed to data collection and analysis. All authors participated in writing and revising the manuscript.

Acknowledgements:

This work was supported by a National Science Foundation CAREER Award 1653160 and NIH 1R01HL136590 (both to S.G.C) and 5R01HL036153 (to W.L.).

Conflict of Interest Disclosure

S.G.C. holds equity ownership in Propria LLC, which has licensed technology used in the research reported in this publication

References

1. Bagnall RD, Weintraub RG, Ingles J, et al. A Prospective Study of Sudden Cardiac Death among Children and Young Adults. *New England Journal of Medicine*. 2016;374(25):2441-2452. doi:10.1056/NEJMoa1510687

2. Watkins H, Ashrafian H, Redwood C. Inherited Cardiomyopathies. *New England Journal of Medicine*. 2011;364(17):1643-1656. doi:10.1056/NEJMra0902923

3. Lu M, Zhao S, Jiang S, et al. Fat deposition in dilated cardiomyopathy assessed by CMR. *JACC Cardiovasc Imaging*. 2013;6(8):889-898. doi:10.1016/j.jcmg.2013.04.010

4. Moore JR, Leinwand L, Warshaw DM, Robbins J, Seidman C, Watkins H. Understanding Cardiomyopathy Phenotypes Based on the Functional Impact of Mutations in the Myosin Motor. *Circulation Research*. 2012;111(3):375-385. doi:10.1161/CIRCRESAHA.110.223842

5. Lu QW, Wu XY, Morimoto S. Inherited cardiomyopathies caused by troponin mutations. *J Geriatr Cardiol*. 2013;10(1):91-101. doi:10.3969/j.issn.1671-5411.2013.01.014

6. Kopylova GV, Shchepkin DV, Borovkov DI, Matyushenko AM. Effect of Cardiomyopathic Mutations in Tropomyosin on Calcium Regulation of the Actin—Myosin Interaction in Skeletal Muscle. *Bull Exp Biol Med*. 2016;162(1):42-44. doi:10.1007/s10517-016-3540-x

7. Jones MR, Tran C, Singh J, Dawson JF. A gradient of force generation at rest differentiates cardiomyopathy outcomes with variants of actin located at the same residue. *Journal of Molecular and Cellular Cardiology Plus*. 2022;2:100023. doi:10.1016/j.jmccpl.2022.100023

8. Schuldt M, Johnston JR, He H, et al. Mutation location of HCM-causing troponin T mutations defines the degree of myofilament dysfunction in human cardiomyocytes. *Journal of Molecular and Cellular Cardiology*. 2021;150:77-90. doi:10.1016/j.yjmcc.2020.10.006

9. Davis J, Davis LC, Correll RN, et al. A Tension-Based Model Distinguishes Hypertrophic versus Dilated Cardiomyopathy. *Cell*. 2016;165(5):1147-1159. doi:10.1016/j.cell.2016.04.002

10. Orzechowski M, Fischer S, Moore JR, Lehman W, Farman GP. Energy landscapes reveal the myopathic effects of tropomyosin mutations. *Archives of Biochemistry and Biophysics*. 2014;564:89-99. doi:10.1016/j.abb.2014.09.007

11. Farman GP, Rynkiewicz MJ, Orzechowski M, Lehman W, Moore JR. HCM and DCM cardiomyopathy-linked α-tropomyosin mutations influence off-state stability and crossbridge interaction on thin filaments. *Arch Biochem Biophys*. 2018;647:84-92. doi:10.1016/j.abb.2018.04.002

12. Bai F, Groth HL, Kawai M. DCM-Related Tropomyosin Mutants E40K/E54K Over-Inhibit the Actomyosin Interaction and Lead to a Decrease in the Number of Cycling Cross-Bridges. *PLoS One*. 2012;7(10):e47471. doi:10.1371/journal.pone.0047471

13. Rajan S, Ahmed RPH, Jagatheesan G, et al. Dilated Cardiomyopathy Mutant Tropomyosin Mice Develop Cardiac Dysfunction With Significantly Decreased Fractional Shortening and Myofilament Calcium Sensitivity. *Circulation Research*. 2007;101(2):205-214. doi:10.1161/CIRCRESAHA.107.148379

14. Lehman W, Rynkiewicz MJ. Troponin-I–induced tropomyosin pivoting defines thin-filament function in relaxed and active muscle. *Journal of General Physiology*. 2023;155(7):e202313387. doi:10.1085/jgp.202313387

15. Haftbaradaran Esfahani P, ElBeck Z, Sagasser S, et al. Cell shape determines gene expression: cardiomyocyte morphotypic transcriptomes. *Basic Res Cardiol*. 2020;115(1):7. doi:10.1007/s00395-019-0765-7

16. Creso JG, Campbell SG. Potential impacts of the cardiac troponin I mobile domain on myofilament activation and relaxation. *J Mol Cell Cardiol*. 2021;155:50-57. doi:10.1016/j.yjmcc.2021.02.012

17. Sewanan LR, Moore JR, Lehman W, Campbell SG. Predicting Effects of Tropomyosin Mutations on Cardiac Muscle Contraction through Myofilament Modeling. *Front Physiol*. 2016;7:473. doi:10.3389/fphys.2016.00473

18. Rynkiewicz MJ, Pavadai E, Lehman W. Modeling Human Cardiac Thin Filament Structures. *Front Physiol*. 2022;13:932333. doi:10.3389/fphys.2022.932333

19. Halder SS, Rynkiewicz MJ, Creso JG, et al. Mechanisms of pathogenicity in the hypertrophic cardiomyopathy-associated TPM1 variant S215L. *PNAS Nexus*. 2023;2(3):pgad011. doi:10.1093/pnasnexus/pgad011

20. Tyska MJ, Hayes E, Giewat M, Seidman CE, Seidman JG, Warshaw DM. Single-molecule mechanics of R403Q cardiac myosin isolated from the mouse model of familial hypertrophic cardiomyopathy. *Circ Res*. 2000;86(7):737-744. doi:10.1161/01.res.86.7.737

21. Debold EP, Schmitt JP, Patlak JB, et al. Hypertrophic and dilated cardiomyopathy mutations differentially affect the molecular force generation of mouse alpha-cardiac myosin in the laser trap assay. *Am J Physiol Heart Circ Physiol*. 2007;293(1):H284-291. doi:10.1152/ajpheart.00128.2007

22. Jongbloed RJ, Marcelis CL, Doevendans PA, et al. Variable clinical manifestation of a novel missense mutation in the alpha-tropomyosin (TPM1) gene in familial hypertrophic cardiomyopathy. *Journal of the American College of Cardiology*. 2003;41(6):981-986. doi:10.1016/S0735-1097(02)03005-X

23. Chang AN, Harada K, Ackerman MJ, Potter JD. Functional Consequences of Hypertrophic and Dilated Cardiomyopathy-causing Mutations in α-Tropomyosin *. *Journal of Biological Chemistry*. 2005;280(40):34343-34349. doi:10.1074/jbc.M505014200

24. Chang AN, Greenfield NJ, Singh A, Potter JD, Pinto JR. Structural and protein interaction effects of hypertrophic and dilated cardiomyopathic mutations in alpha-tropomyosin. *Frontiers in Physiology*. 2014;5. Accessed October 27, 2023. https://www.frontiersin.org/articles/10.3389/fphys.2014.00460

25. Zheng W, Hitchcock-DeGregori SE, Barua B. Investigating the effects of tropomyosin mutations on its flexibility and interactions with filamentous actin using molecular dynamics simulation. *J Muscle Res Cell Motil*. 2016;37(4):131-147. doi:10.1007/s10974-016-9447-3

26. Gupte TM, Haque F, Gangadharan B, et al. Mechanistic Heterogeneity in Contractile Properties of α-Tropomyosin (TPM1) Mutants Associated with Inherited Cardiomyopathies. *J Biol Chem*. 2015;290(11):7003-7015. doi:10.1074/jbc.M114.596676

27. Sewanan LR, Park J, Rynkiewicz MJ, et al. Loss of crossbridge inhibition drives pathological cardiac hypertrophy in patients harboring the TPM1 E192K mutation. *J Gen Physiol*. 2021;153(9):e202012640. doi:10.1085/jgp.202012640

28. Sequeira V, Wijnker PJM, Nijenkamp LLAM, et al. Perturbed Length–Dependent Activation in Human Hypertrophic Cardiomyopathy With Missense Sarcomeric Gene Mutations. *Circ Res*. 2013;112(11):1491-1505. doi:10.1161/CIRCRESAHA.111.300436

29. Clippinger SR, Cloonan PE, Greenberg L, Ernst M, Stump WT, Greenberg MJ. Disrupted mechanobiology links the molecular and cellular phenotypes in familial dilated cardiomyopathy. *Proceedings of the National Academy of Sciences*. 2019;116(36):17831-17840. doi:10.1073/pnas.1910962116

30. Olson TM, Kishimoto NY, Whitby FG, Michels VV. Mutations that Alter the Surface Charge of Alpha-tropomyosin are Associated with Dilated Cardiomyopathy. *Journal of Molecular and Cellular Cardiology*. 2001;33(4):723-732. doi:10.1006/jmcc.2000.1339

31. Mirza M, Marston S, Willott R, et al. Dilated Cardiomyopathy Mutations in Three Thin Filament Regulatory Proteins Result in a Common Functional Phenotype *. *Journal of Biological Chemistry*. 2005;280(31):28498-28506. doi:10.1074/jbc.M412281200

32. Memo M, Leung MC, Ward DG, et al. Familial dilated cardiomyopathy mutations uncouple troponin I phosphorylation from changes in myofibrillar Ca2+ sensitivity. *Cardiovascular Research*. 2013;99(1):65-73. doi:10.1093/cvr/cvt071

33. Schwinger RH, Böhm M, Koch A, et al. The failing human heart is unable to use the Frank-Starling mechanism. *Circ Res*. 1994;74(5):959-969. doi:10.1161/01.RES.74.5.959

34. Nagueh SF, Shah G, Wu Y, et al. Altered Titin Expression, Myocardial Stiffness, and Left Ventricular Function in Patients With Dilated Cardiomyopathy. *Circulation*. 2004;110(2):155-162. doi:10.1161/01.CIR.0000135591.37759.AF

35. Makarenko I, Opitz C a., Leake M c., et al. Passive Stiffness Changes Caused by Upregulation of Compliant Titin Isoforms in Human Dilated Cardiomyopathy Hearts. *Circulation Research*. 2004;95(7):708-716. doi:10.1161/01.RES.0000143901.37063.2f

36. Boogerd CJ, Perini I, Kyriakopoulou E, et al. Cardiomyocyte proliferation is suppressed by ARID1A-mediated YAP inhibition during cardiac maturation. *Nat Commun*. 2023;14(1):4716. doi:10.1038/s41467-023-40203-2

37. Zeng N, Huang YQ, Yan YM, et al. Diverging targets mediate the pathological role of miR-199a-5p and miR-199a-3p by promoting cardiac hypertrophy and fibrosis,. *Molecular Therapy - Nucleic Acids,*. 2021;26:1035-1050. doi:https://doi.org/10.1016/j.omtn.2021.10.013.

38. Gupta MP, Gupta M, Dizon E, Zak R. Sympathetic control of cardiac myosin heavy chain gene expression. *Mol Cell Biochem*. 1996;157(1):117-124. doi:10.1007/BF00227889

39. Jiang SW, Dong M, Trujillo MA, Miller LJ, Eberhardt NL. DNA Binding of TEA/ATTS Domain Factors Is Regulated by Protein Kinase C Phosphorylation in Human Choriocarcinoma Cells *. *Journal of Biological Chemistry*. 2001;276(26):23464-23470. doi:10.1074/jbc.M010934200

40. Wolfram JA, Lesnefsky EJ, Hoit BD, Smith MA, Lee H gon. Therapeutic Potential of c-Myc Inhibition in the Treatment of Hypertrophic Cardiomyopathy. *Ther Adv Chronic Dis*. 2011;2(2):133-144. doi:10.1177/2040622310393059

41. Chen QM, Maltagliati AJ. Nrf2 at the heart of oxidative stress and cardiac protection. *Physiol Genomics*. 2018;50(2):77-97. doi:10.1152/physiolgenomics.00041.2017

42. Lotto J, Cullum R, Drissler S, et al. Cell diversity and plasticity during atrioventricular heart valve EMTs. *Nat Commun*. 2023;14(1):5567. doi:10.1038/s41467-023-41279-6

43. Mihl C, Dassen WRM, Kuipers H. Cardiac remodelling: concentric versus eccentric hypertrophy in strength and endurance athletes. *Neth Heart J*. 2008;16(4):129-133.

44. Li X (Edward), Suphamungmee W, Janco M, et al. The flexibility of two tropomyosin mutants, D175N and E180G, that cause hypertrophic cardiomyopathy. *Biochem Biophys Res Commun*. 2012;424(3):493-496. doi:10.1016/j.bbrc.2012.06.141

45. Sundar S, Rynkiewicz MJ, Ghosh A, Lehman W, Moore JR. Cardiomyopathy Mutation Alters End-to-End Junction of Tropomyosin and Reduces Calcium Sensitivity. *Biophys J*. 2020;118(2):303-312. doi:10.1016/j.bpj.2019.11.3396

46. Desai MY, Owens A, Wolski K, et al. Mavacamten in Patients With Hypertrophic Cardiomyopathy Referred for Septal Reduction: Week 56 Results From the VALOR-HCM Randomized Clinical Trial. *JAMA Cardiology*. 2023;8(10):968-977. doi:10.1001/jamacardio.2023.3342

47. Sebastian SA, Padda I, Lehr EJ, Johal G. Aficamten: A Breakthrough Therapy for Symptomatic Obstructive Hypertrophic Cardiomyopathy. *Am J Cardiovasc Drugs*. 2023;23(5):519-532. doi:10.1007/s40256-023-00599-0

48. Teerlink JR, Diaz R, Felker GM, et al. Cardiac Myosin Activation with Omecamtiv Mecarbil in Systolic Heart Failure. *New England Journal of Medicine*. 2021;384(2):105-116. doi:10.1056/NEJMoa2025797

49. Voors AA, Tamby J, Cleland JG, et al. Effects of danicamtiv, a novel cardiac myosin activator, in heart failure with reduced ejection fraction: experimental data and clinical results from a phase 2a trial. *Eur J Heart Fail*. 2020;22(9):1649-1658. doi:10.1002/ejhf.1933

50. Lian X, Zhang J, Azarin SM, et al. Directed cardiomyocyte differentiation from human pluripotent stem cells by modulating Wnt/β-catenin signaling under fully defined conditions. *Nat Protoc*. 2013;8(1):162-175. doi:10.1038/nprot.2012.150

51. Schwan J, Kwaczala AT, Ryan TJ, et al. Anisotropic engineered heart tissue made from laser-cut decellularized myocardium. *Sci Rep*. 2016;6(1):32068. doi:10.1038/srep32068

52. Sewanan LR, Schwan J, Kluger J, et al. Extracellular Matrix From Hypertrophic Myocardium Provokes Impaired Twitch Dynamics in Healthy Cardiomyocytes. *JACC: Basic to Translational Science*. 2019;4(4):495-505. doi:10.1016/j.jacbts.2019.03.004

53. Stull LB, Leppo MK, Marbán E, Janssen PML. Physiological determinants of contractile force generation and calcium handling in mouse myocardium. *J Mol Cell Cardiol*. 2002;34(10):1367-1376. doi:10.1006/jmcc.2002.2065

54. Li XE, Holmes KC, Lehman W, Jung H, Fischer S. The shape and flexibility of tropomyosin coiled coils: implications for actin filament assembly and regulation. *J Mol Biol*. 2010;395(2):327-339. doi:10.1016/j.jmb.2009.10.060

55. Lorenz M, Poole KJ, Popp D, Rosenbaum G, Holmes KC. An atomic model of the unregulated thin filament obtained by X-ray fiber diffraction on oriented actin-tropomyosin gels. *J Mol Biol*. 1995;246(1):108-119. doi:10.1006/jmbi.1994.0070

56. Rynkiewicz MJ, Schott V, Orzechowski M, Lehman W, Fischer S. Electrostatic interaction map reveals a new binding position for tropomyosin on F-actin. *J Muscle Res Cell Motil*. 2015;36(6):525-533. doi:10.1007/s10974-015-9419-z

57. Humphrey W, Dalke A, Schulten K. VMD: Visual molecular dynamics. *Journal of Molecular Graphics*. 1996;14(1):33-38. doi:10.1016/0263-7855(96)00018-5

58. Phillips JC, Hardy DJ, Maia JDC, et al. Scalable molecular dynamics on CPU and GPU architectures with NAMD. *J Chem Phys*. 2020;153(4):044130. doi:10.1063/5.0014475

59. Hinkley DV. Bootstrap Methods. *Journal of the Royal Statistical Society: Series B (Methodological)*. 1988;50(3):321-337. doi:10.1111/j.2517-6161.1988.tb01731.x

Figures

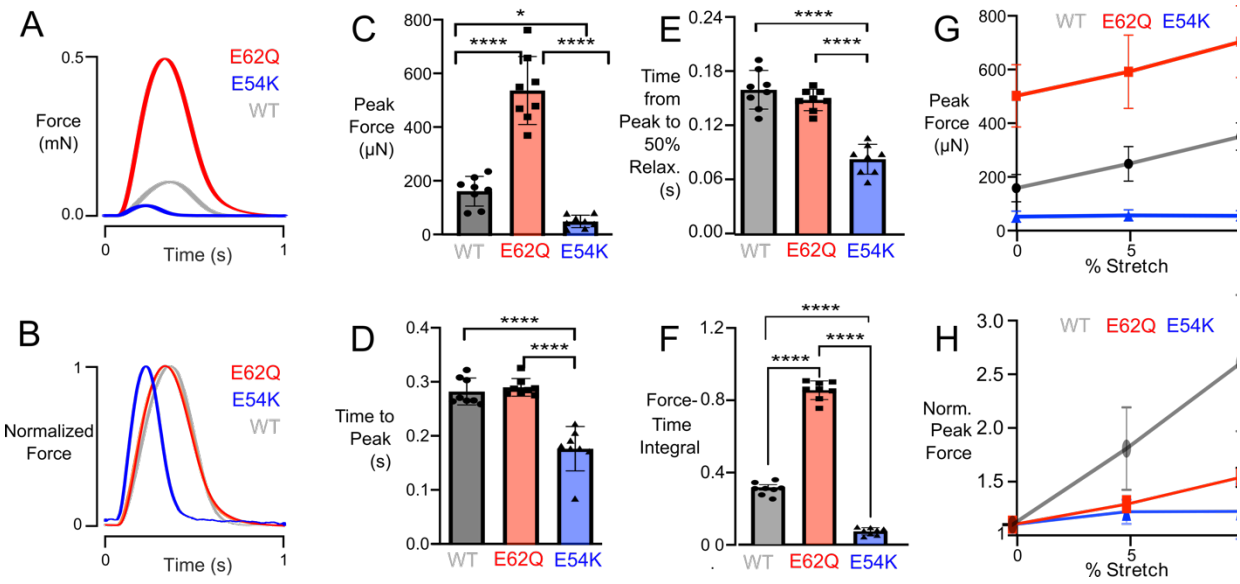

Figure 1: Basic twitch properties of WT, E62Q and E54K EHTs while pacing at 1 Hz. (A-B) Sample force traces, (C) Peak force, (D) Time from start of stimulus to peak force (E) Time from peak to 50% relaxation (F) Force-Time Integral (FTI) (G) Length dependent activation of EHTs showing peak forces at 0%, 5% and 10% stretch. No statistical test performed (H) Length dependent activation of EHTs showing normalized peak forces (data from each EHT normalized to its own peak force at culture length i.e., 0% stretch). E62Q and E54K Curve significantly different from WT by Two-way ANOVA with multiple comparisons at 5% stretch ($p = 0.0156$ and $p= 0.0076$ respectively) and at 10% stretch ($p = 0.051$ and $p= 0.0007$ respectively).

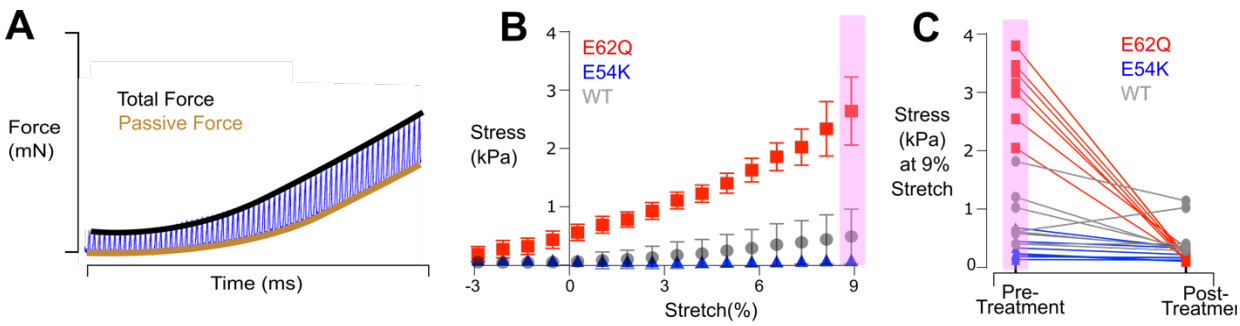

Figure 2: Diastolic stiffness. (A) Sample force trace during stretch. (B) Passive stress in WT, E62Q and E54K EHTs (N= 8) E62Q passive stress is significantly different from E54K and WT using 2-way ANOVA. (C) Passive stress in WT, E62Q and E54K EHTs at 9% stretch before and after 30 min of 2 µM mavacamten treatment [N =8, passive stress values are significantly different using 2-way ANOVA with multiple comparisons (p value = 0.0001); significant interaction between genotype and mavacamten treatment.]

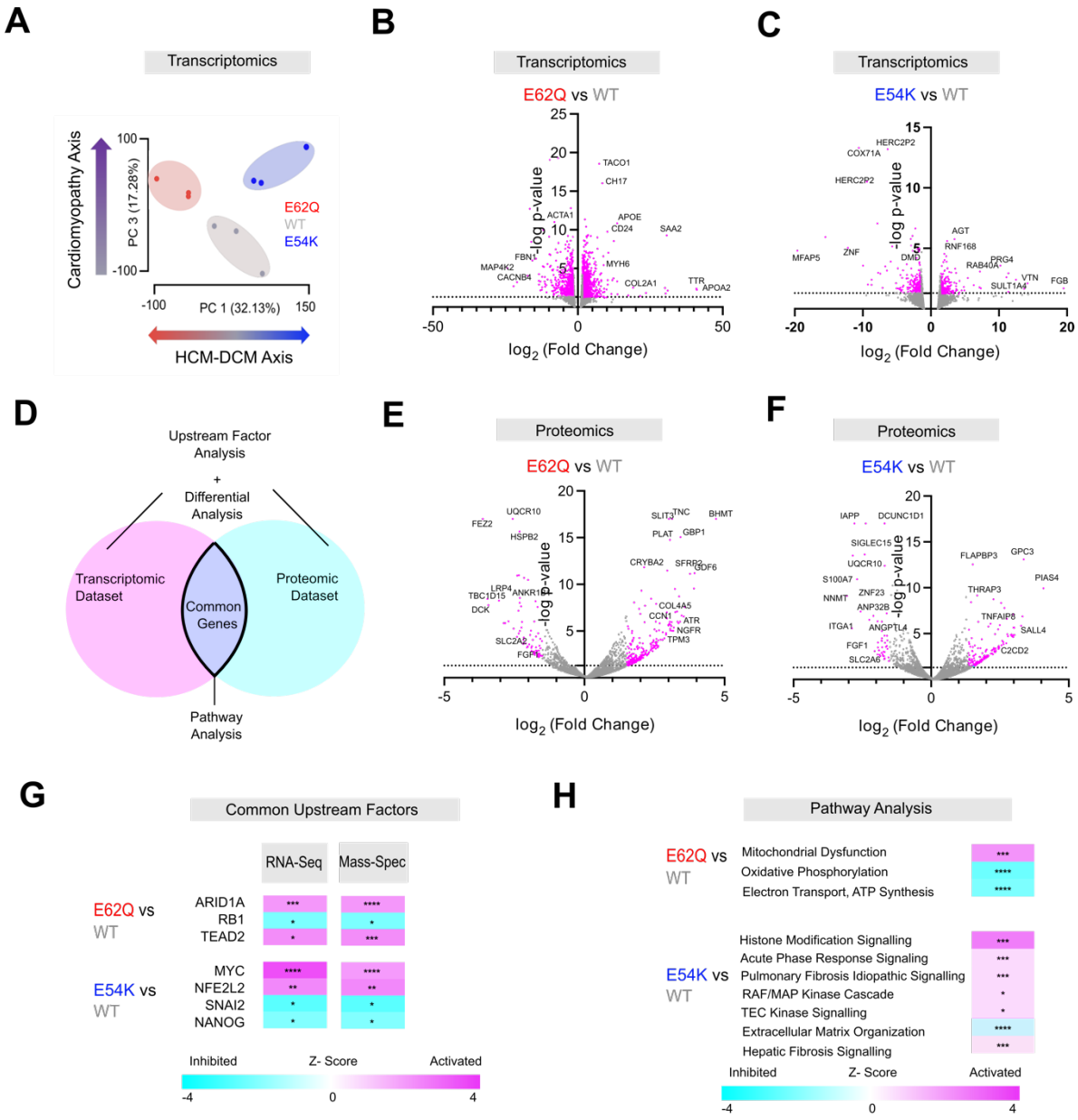

Figure 3: Transcriptomic and Proteomic Analysis of EHTs. (A) Exploratory Principal Component Analysis of the transcriptomic data (Bulk RNA-Seq) where each point represents a unique sample. (B) Volcano plots from RNA-Seq analysis of differentially regulated genes in E62Q vs WT comparison. (C) Volcano plots from RNA-Seq analysis of differentially regulated genes in E54K vs WT comparison. The full dataset is available on Gene Expression Omnibus (GEO) database under accession ID GSE251993. (D) Schematic to explain how the transcriptomic and proteomic datasets were used for different types of analysis. (E) Volcano plots from Mass Spectrometry data of differentially regulated proteins in E62Q vs WT comparison. (F) Volcano plots from Mass Spectrometry data of differentially regulated proteins in E54K vs WT comparison. (G) Common upstream transcription factors from independent upstream analysis of proteomic and transcriptomic data. (H) Top canonical pathways identified by Ingenuity Pathway Analysis using common set of genes from proteomic and transcriptomic datasets.

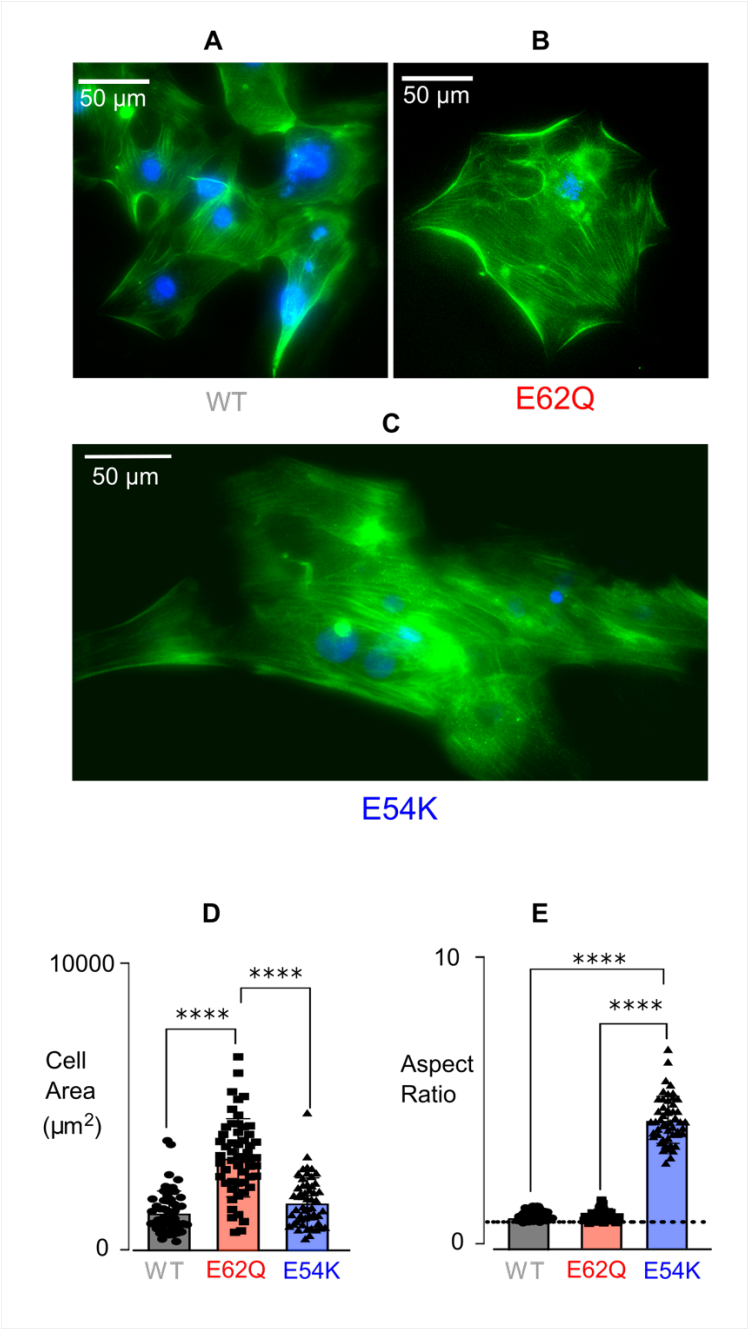

Figure 4: Cell size measurements. cTnT (green) and DAPI (blue) staining of (A) WT, (B) E62Q and (C) E54K iPSC-CM cells. (D) cell area and (E) aspect ratio measurements. Statistical Analysis: One-Way ANOVA with multiple comparisons, p-values for multiple comparisons are indicated on the figures using asterisks ($p < 0.0001$).

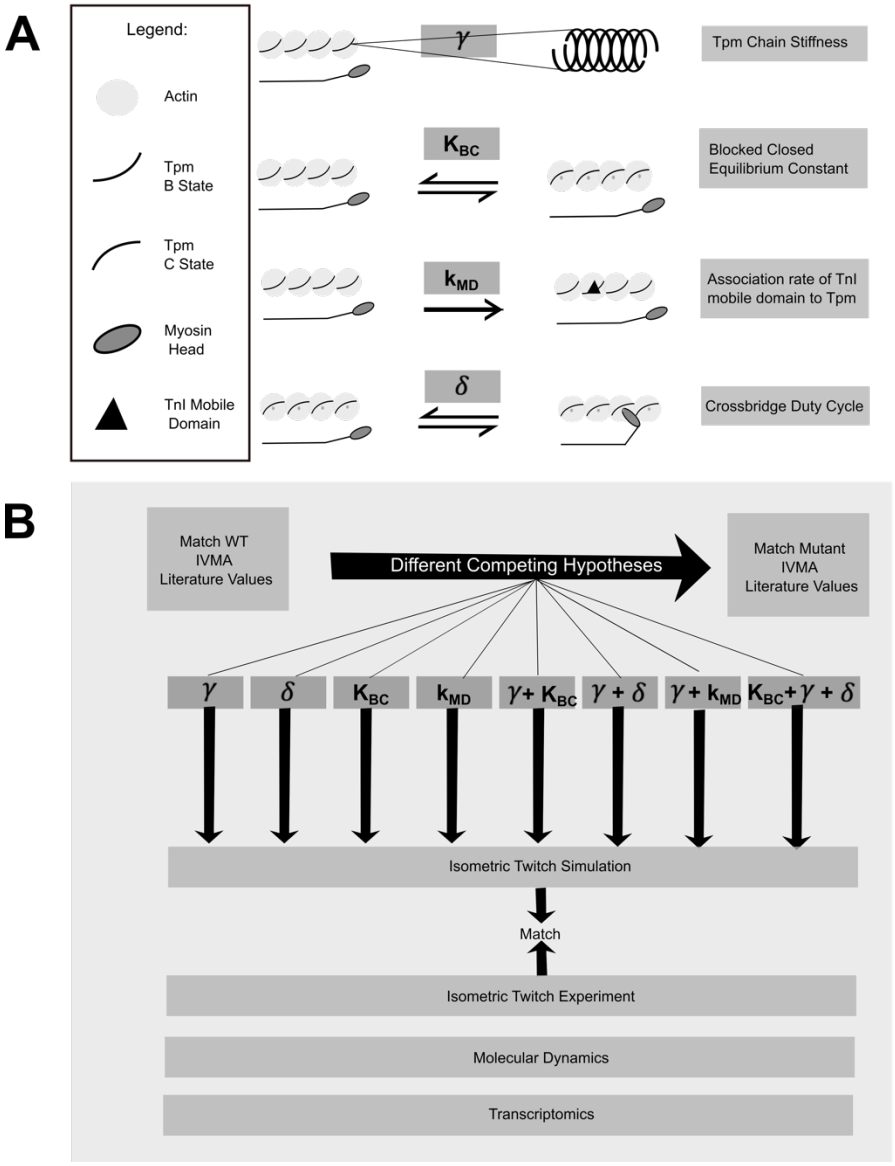

Figure 5: Hypothesis Driven Approach. (A) Tunable Parameters Used in the Simulations. (B) Evaluation of Several Competing Hypotheses.

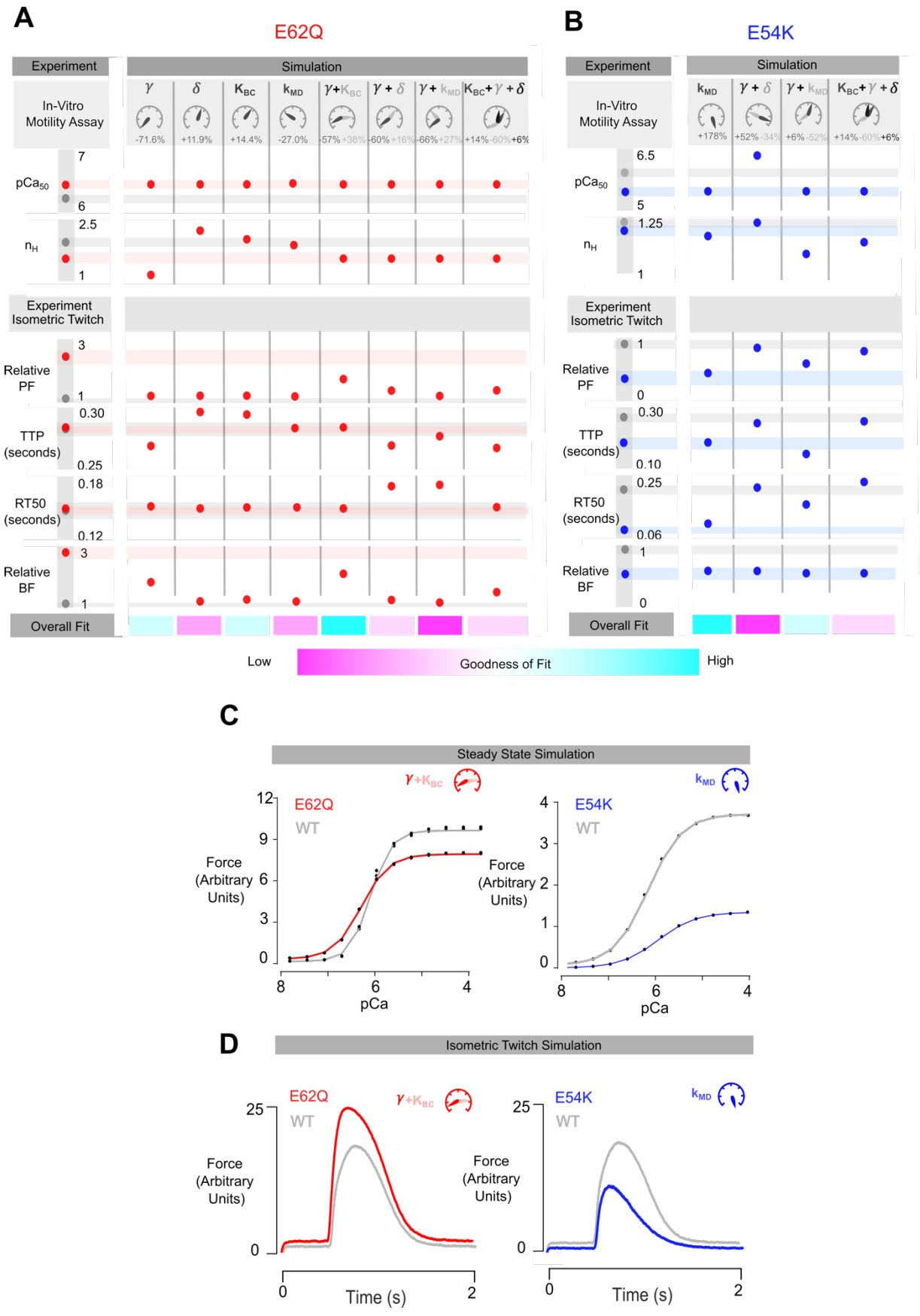
A
E62Q
Experiment
Simulation
In-Vitro Motility Assay
γ
δ
K_BC
k_MD
γ+K_BC
γ + δ
γ + k_MD
K_BC+γ + δ
-71.6%
+11.9%
+14.4%
-27.0%
-57% +38%
-60% +16%
-66% +27%
+14% -60% +6%
pCa50
nH
Experiment Isometric Twitch
Relative PF
TTP (seconds)
RT50 (seconds)
Relative BF
Overall Fit
B
E54K
k_MD
γ + δ
γ + k_MD
K_BC+γ + δ
+178%
+52% -34%
+6% -52%
+14% -60% +6%
Low
Goodness of Fit
High
C
Steady State Simulation
E62Q
WT
E54K
Force (Arbitrary Units)
pCa
D
Isometric Twitch Simulation
Time (s)

Figure 6: Computational simulations. Speedometer graphics show the direction and magnitude of parameter changes (not to scale). Gray, red, and blue shaded horizontal bars represent the standard deviations of experimental datasets for WT, E62Q and E54K EHTs respectively. Gray, red, and blue dots represent the mean of experimental datasets and output of computational simulations for WT, E62Q and E54K EHTs respectively. An ideal match would show dots inside of all the bars of the same color.
(A) Steady state (top) and twitch simulation (bottom) result summary for E62Q.
(B) Steady state (top) and twitch simulation (bottom) result summary for E54K
(C) Steady state simulations for the winning hypotheses (γ + K_{BC} for E62Q and k_{MD} for E54K) in each case
(D) Isometric twitch simulations for the winning hypotheses (γ + K_{BC} for E62Q and k_{MD} for E54K) in each case

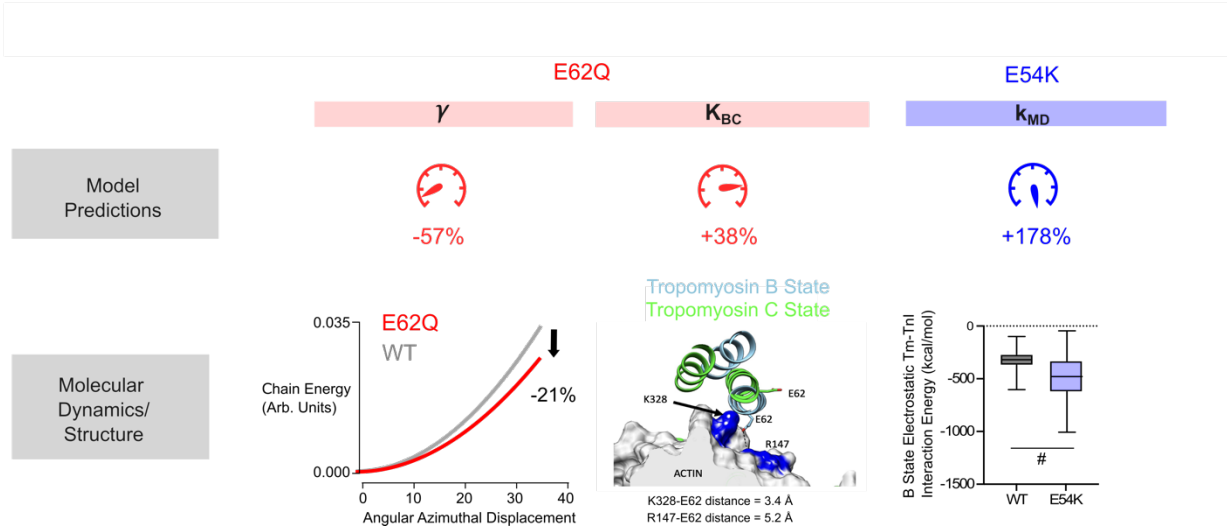

Figure 7: Left: Chain energy vs. azimuthal displacement showing decreased effective stiffness of E62Q calculated using the 2D coarse-grain model. Center: PDB structures of E62 tropomyosin in low and high calcium. Right: Tropomyosin-Troponin I Interaction Energy in the B state of WT and E54K tropomyosin. (Averaged over n= 1000 frames for WT and n=3000 frames for E54K, error bars represent standard deviation, # indicates results significantly different using bootstrapping to analyze of difference of means. In this case 11 out of 10000 repeated samplings with replacement showed no difference between means (equivalent to p-value of 0.0011).

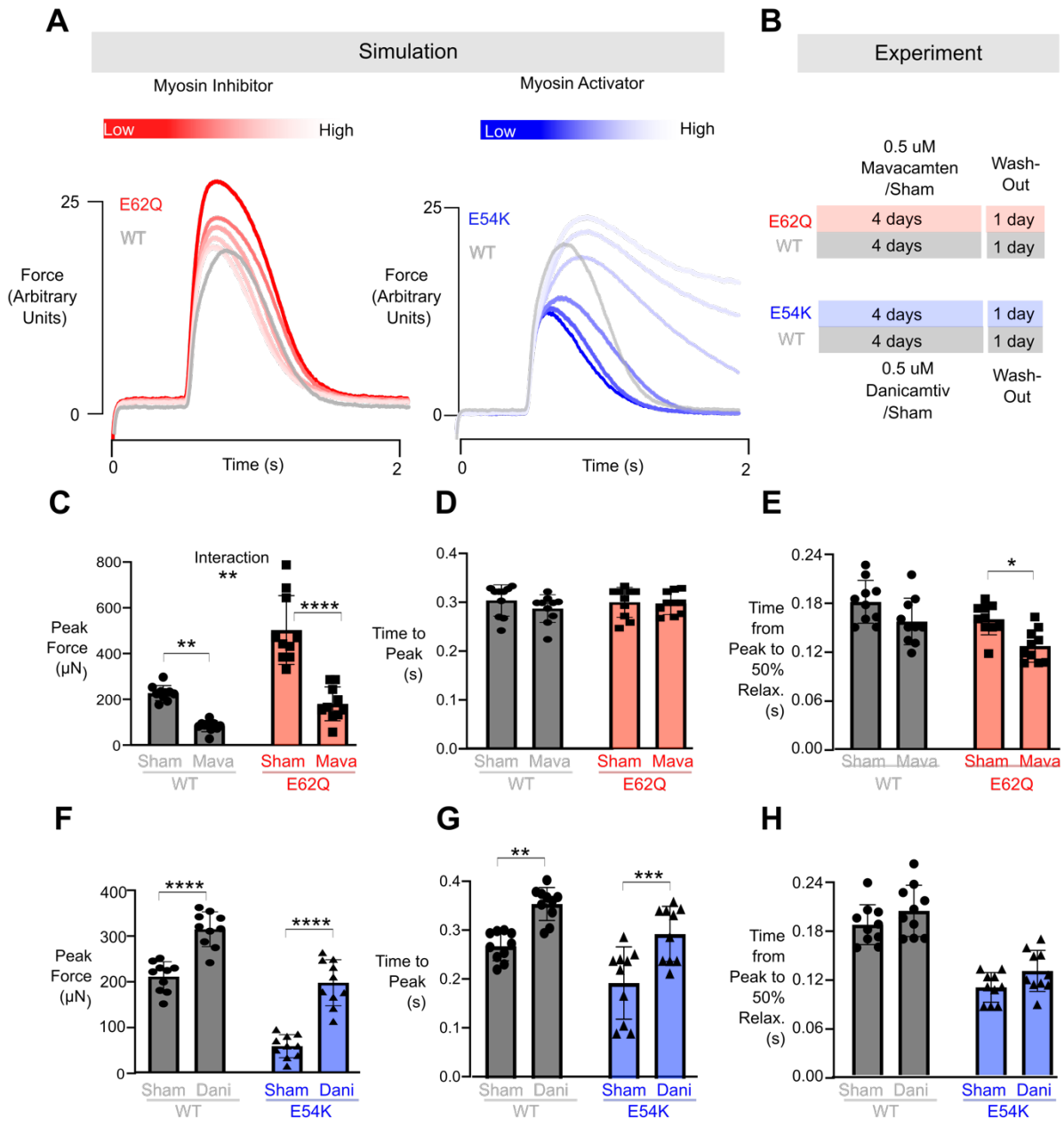

Figure 8: Drug Treatment of EHTs. (A) Simulation of myosin modulators (B) Experimental Plan. (C) Peak Force (D) Time To Peak and (E) Time to Relax to 50% for E62Q/WT EHTs with Mavacamten/Sham. (F) Peak Force (G) Time To Peak and (H) Time to Relax to 50% for E54K/WT EHTs with Danicamtiv/Sham. Statistical Analysis: Two-Way ANOVA with multiple comparisons, p-values for multiple comparisons are indicated on the figures using asterisks.

Tables

Table 1: Summary of Experimental Results in Previous Literature

Genotype	In Vitro Motility Assay	
	% ΔpCa_{50} shift from WT	**% Δn_H shift from WT**
E62Q	+3% (Farman et al, 2018)	-25% (Farman et al, 2018)
E54K	-5% (Bai et al, 2012)	0% (Bai et al, 2012)

Table 2: Parameters used in the isometric twitch simulations of each hypothesis. Top values are for E62Q, and bottom values are for E54K for each parameter where there are multiple entries. A dash (-) indicates that the simulation was not run for E54K.

Parameter	WT	γ	δ	K_{BC}	k_{MD}	γ + K_{BC}	γ + δ	γ + k_{MD}	K_{BC} + γ + δ
$k_{Ca}^{+}\ (\mu M^{-1}s^{-1})$	275	275	275	275	275	275	275	275	275
$k_{Ca}^{-}(s^{-1})$	1575	1575	1575	1575	1575	1575	1575	1575	1575
$k_{SP}^{+}(s^{-1})$	225	225	225	225	225	225	225	225	225
$k_{SP}^{-}(s^{-1})$	292.5	292.5	292.5	292.5	292.5	292.5	292.5	292.5	292.5
$k_{IP}^{+}(s^{-1})$	1777.5	1777.5	1777.5	1777.5	1777.5	1777.5	1777.5	1777.5	1777.5
$k_{IP}^{-}(s^{-1})$	225	225	225	225	225	225	225	225	225
$k_{MD}^{+}(s^{-1})$	1462.5	1462.5	1462.5	1462.5	1462.5	1462.5	1462.5	1462.5	1462.5
$k_{MD}^{-}(s^{-1})$	225	225 -	225 -	225 -	164.25 612	225 -	225 225	164.25 319.5	225 225
$k_{ref}^{BC}(s^{-1})$	675	675	675	675	675	675	675	675	675
K_{BC}	2	2 -	2 -	2.288 -	2 2	2.76 -	2 2	2 2	2.28 1.84
$f_{XY}(s^{-1})$	225	225	225	225	225	225	225	225	225
δ	0.48	0.48 -	0.537 -	0.48 -	0.48 0.48	0.48 -	0.5568 0.3168	0.48 0.4225	0.5088 0.4080
λ	0.001	0.001	0.001	0.001	0.001	0.001	0.001	0.001	0.001
η	16	16	16	16	16	16	16	16	16
μ	16	16	16	16	16	16	16	16	16
$\gamma(mol^{-1}kJ)$	70	19.88 -	70 -	70 -	70 70	30.1 -	28 106.4	23.8 74.2	28 106.4